



Available online at www.keaipublishing.com/en/journals/journal-of-magnesium-and-alloys/

ScienceDirect

Journal of Magnesium and Alloys 13 (2025) 3617–3631



www.elsevier.com/locate/jma

Full Length Article

Texture-dependent bending behaviors of extruded AZ31 magnesium alloy plates [☆]

Kecheng Zhou^{a,b}, Xiaochuan Sun^{a,d}, Hongwei Wang^b, Xiaodan Zhang^a, Ding Tang^{a,*}, Weiqin Tang^a, Yaodong Jiang^b, Peidong Wu^c, Huamiao Wang^{a,b,d,*}

^a State Key Laboratory of Mechanical System and Vibration, Shanghai Jiao Tong University, Shanghai 200240, China
^b State Key Laboratory for GeoMechanics and Deep Underground Engineering, China University of Mining & Technology, Beijing 100083, China

^c Department of Mechanical Engineering, McMaster University, Hamilton, ON L8S 4L7, Canada

^d Materials Genome Initiative Center, Shanghai Jiao Tong University, Shanghai 200240, China

Received 19 September 2022; received in revised form 4 January 2023; accepted 1 February 2023 Available online 6 March 2023

Abstract

The relatively insufficient knowledge of the deformation behavior has limited the wide application of the lightest structure material-Mg alloys. Among others, bending behavior is of great importance because it is unavoidably involved in various forming processes, such as folding, stamping, etc. The hexagonal close-packed structure makes it even a strong texture-dependent behavior and even hard to capture and predict. In this regard, the bending behaviors are investigated in terms of both experiments and simulations in the current work. Bending samples with longitudinal directions inclined from the transverse direction by different angles have been prepared from an extruded AZ31 plate, respectively. The moment-curvature curves and strain distribution have been recorded in the four-point bending tests assisted with an *in-situ* digital image correlation (DIC) system. A crystal-plasticity-based bending-specific approach named EVPSC-BEND was applied to bridge the mechanical response to the microstructure evolution and underlying deformation mechanisms. The flow stress, texture, twin volume fraction, stress distribution, and strain distribution evolve differently from sample to sample, manifesting strong texture-dependent bending behaviors. The underlying mechanisms associated with this texture dependency, especially the occurrence of both twinning and detwinning during the monotonic bending, are carefully discussed. Besides, the simulation has been conducted to reveal the moment-inclination angle relation of the investigated AZ31 extruded plate in terms of the polar coordinate, which intuitively shows the texture-dependent behaviors. Specifically, the samples with longitudinal directions parallel to the extruded direction bear the biggest initial yielding moment.

© 2023 Chongqing University. Publishing services provided by Elsevier B.V. on behalf of KeAi Communications Co. Ltd.

This is an open access article under the CC BY-NC-ND license (http://creativecommons.org/licenses/by-nc-nd/4.0/)

Keywords: Magnesium alloy; Bending; Texture-dependency; Crystal plasticity; Twinning and detwinning.

1. Introduction

Magnesium (Mg) alloys draw worldwide attention with their lightweight, high specific strength, and excellent recyclability [1–4]. The inherent hexagonal close-packed (HCP) structure, the unidirectional deformation mechanism of twinning, and the developed texture result in the strongly

anisotropic behavior of wrought Mg alloy [5–8]. To accommodate arbitrary deformation, at least five independent deformation systems are indispensable. In the case of Mg alloys, basal < a> slip ($\{0001\}11\bar{2}0\}$) [9], prismatic < a> slip ($\{10\bar{1}0\}11\bar{2}0\}$) [10], pyramidal < a> slip ($\{10\bar{1}1\}11\bar{2}0\}$) [11], pyramidal < a> slip ($\{10\bar{1}2\}11\bar{2}3\}$) [12] and extension twin ($\{10\bar{1}2\}10\bar{1}1\}$) [13] are the major deformation mechanisms that have been observed experimentally. The initial texture plays a vital role in the plastic deformation of Mg alloys and strongly affects the strength and formability [6,14–17], where the extension twin takes the primary responsibility because of its polar nature. Various factors including temperature, strain

[☆] Peer review under the responsibility of Chongqing University.

^{*} Corresponding authors at: State Key Laboratory of Mechanical System and Vibration, Shanghai Jiao Tong University, Shanghai 200240, China.

E-mail addresses: tangding@sjtu.edu.cn (D. Tang), wanghm02@sjtu.edu.cn (H. Wang).

rate, and texture have been investigated in either homogenous loading cases [6,18–22] or inhomogeneous ones [23–28]. As an inhomogeneous case, bending behavior is very common in usual manufacturing processes or in-service conditions [29–31]. However, the influence of the initial texture on the bending behaviors of Mg alloys, especially their quantitative relationship, still remains obscure. Therefore, understanding and quantifying the texture-dependent bending behaviors of Mg alloys are invaluable in the advancement of processing technology and product quality.

The bending behaviors and the corresponding mechanisms of Mg alloys have been studied experimentally or numerically [24,31-35]. Huang et al. [33] studied the bending behavior of AZ31 Mg alloy sheets with a strong basal texture subjected to V-bending. They found that the neutral layer of the sheet shifted towards the outer region because different deformation mechanisms were activated in the outer and inner regions. Twinning dominated the inner region (under compression) while the prismatic slip dominated the outer region (under tension). Singh et al. [31,34,36] found that both tensile and compressive twinning were active in the Mg alloys under a mini-V-bending test. With EBSD analysis, they found the deformation twinning is more prominent in the E-form alloy than AZ31, which indicates the texture-dependent behavior of the deformation activity. Besides the experiments, they confirmed the activities of both tensile and compressive twins in E-form and AZ31 Mg alloys through simulations in terms of the crystal plasticity finite element method (CPFEM).

In addition to V-bending, researchers have investigated the deformation behavior of Mg alloys subjected to three-point bending experimentally [23,24,32]. Ren et al. [32] illustrated the dependence of neutral layer shifting on the initial texture of AZ31 sheets through an empirical k-value, i.e., the coefficient of the neutral layer. This phenomenon was qualitatively correlated to the physical mechanisms that occurred within the material with the aid of viscoplastic self-consistent (VPSC) simulations. Desinghege et al. [35] experimentally investigated the bending behaviors of AZ31 sheets under both pure bending and V-bending to validate their analytical equation in the estimation of the springback effect. As a function of the experimentally determined yield strength and the shifting of the neutral layer, the analytical relation has implicitly taken into account both the effects of grain size and sample direction, i.e., initial texture. However, a deep understanding of the bending behaviors associated with the underlying physical mechanisms is apparently lacking. Clearly, the bending behaviors of Mg alloys are highly relevant to the operative deformation mechanism and the microstructure. As demonstrated in many studies, the texture, as an important indicator of the microstructure, affects the mechanical response of Mg alloys under tension, compression, and torsion. However, the influence of initial texture on the bending behaviors is less investigated. Though the bending behaviors of AZ31 Mg alloy sheets with weak and strong basal textures have been tackled by Singh et al. [31,34,36], the reported results are affected not only by the initial texture, but also by the grain size. Consequently, to better understand the effect of texture, the bending behaviors of Mg alloys need to be investigated exclusively on the initial textures that are sufficiently different.

In the current works, four bending beams were wire cut from an extruded Mg alloy plate with beam directions oriented differently from the extrusion direction (ED). Bending tests have been performed on different beams to isolate the effect of initial texture on the bending behaviors of Mg alloys, given that other microstructures of the beams remain identical. The inhomogeneous deformation is recorded in-situ in terms of the digital image correlation (DIC) technique during the bending tests. In parallel, the bending behaviors have been simulated by the recently developed crystal plasticitybased bending-specific approach, the elasto-viscoplastic selfconsistent model designed for bending loads (EVPSC-BEND) [37]. Four-point bending tests have been performed on the specimens with various initial textures, which are fabricated with their longitudinal directions (LD) inclined differently from the transverse direction of the extruded plate (e.g., with the inclination angle of 0°, 30°, 45°, and 90°). The DIC technique was employed to measure the strain distribution, loading curvature, and shifting of the neutral layer. After fitting the experimental results by the numerical calculation performed via the EVPSC-BEND method, based on the obtained moment-curvature curves, the texture evolution, the twin volume fraction, and the relative activities of various deformation mechanisms, the effect of initial texture on the bending behaviors of Mg alloys are discussed.

2. Problem formulation and method of solution

The EVPSC-BEND approach to simulate pure bending is briefly described here, the complete description can be found elsewhere [37]. Fig. 1 shows the discretized description of a beam under pure bending. The brown dash line represents the

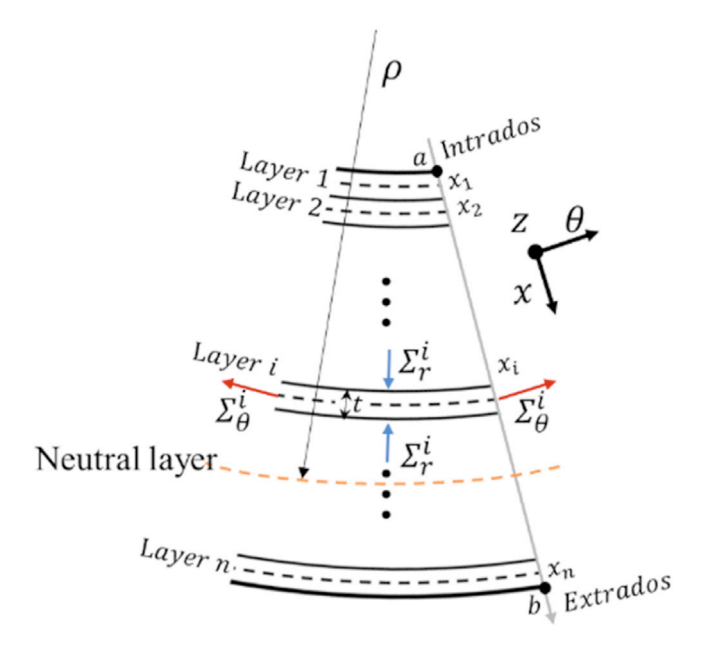


Fig. 1. Discretized description of pure bending.

neutral layer with a curvature of $1/\rho$. A local coordinate (x) along the radius direction is assigned in the beam with the origin at the neutral layer. The coordinates of intrados and extrados are respectively a and b.

The circumferential strain component at Layer i is $E_{\theta}^{i} = x_{i}/\rho$ and in an incremental form as $\Delta E_{\theta}^{i} = -\frac{x^{i}\Delta\rho}{\rho^{2}}$. The increment consists of elastic and plastic parts ΔE_{θ}^{ei} , and ΔE_{θ}^{pi} :

$$\Delta E_{\theta}^{ei} = \Delta E_{\theta}^{i} - \Delta E_{\theta}^{pi} = \bar{M}_{\theta r}^{ei} \Delta \Sigma_{r}^{i} + \bar{M}_{\theta \theta}^{ei} \Delta \Sigma_{\theta}^{i} \tag{1}$$

where, $\bar{M}_{\theta r}^{ei}$ and $\bar{M}_{\theta \theta}^{ei}$ are the components of elastic compliance, and ΔE_{θ}^{pi} is the plastic strain increment of the i^{th} layer. The update of these terms can be accomplished by the crystal plasticity-based elastic viscoplastic self-consistent model with twinning and de-twinning (EVPSC-TDT), which assumes each layer as a homogeneous effective medium (HEM) that could consist of thousands of grains.

The non-zero stress components $\Sigma_{\theta}(x)$ and $\Sigma_{r}(x)$ have to satisfy the equilibrium equation:

$$\Sigma_r(x) = \frac{1}{\rho + x} \int_a^x \Sigma_{\theta}(s) ds \tag{2}$$

Through discretizing Eq. (2) into summation over layers, the stress increment in the beam responding to the bending $(\Delta \rho)$ can be well described by:

$$\begin{bmatrix} \frac{t\tilde{M}_{\theta r}^{e1}}{\rho + x_{1}} + \bar{M}_{\theta \theta}^{ei} & 0 & \cdots & 0 \\ \frac{t\tilde{M}_{\theta r}^{e2}}{\rho + x_{2}} & \frac{t\tilde{M}_{\theta r}^{e2}}{\rho + x_{2}} + \bar{M}_{\theta \theta}^{e2} & \cdots & 0 \\ \vdots & \vdots & \ddots & \vdots \\ \frac{t\tilde{M}_{\theta r}^{en}}{\rho + x_{n}} & \frac{t\tilde{M}_{\theta r}^{en}}{\rho + x_{n}} & \cdots & \frac{t\tilde{M}_{\theta r}^{en}}{\rho + x_{n}} + \bar{M}_{\theta \theta}^{en} \end{bmatrix} \begin{bmatrix} \Delta \Sigma_{\theta}^{1} \\ \Delta \Sigma_{\theta}^{2} \\ \vdots \\ \Delta \Sigma_{\theta}^{n} \end{bmatrix}$$

$$= \begin{bmatrix} \left(\frac{t\tilde{M}_{\theta_{r}}^{e_{1}}}{(\rho+x_{2})^{2}}\sum_{\theta}^{1}-\frac{x_{1}}{\rho^{2}}\right)\Delta\rho - \Delta E_{\theta}^{p_{1}} \\ \left(\frac{t\tilde{M}_{\theta_{r}}^{e_{2}}}{(\rho+x_{2})^{2}}\sum_{k=1}^{2}\sum_{\theta}^{k}-\frac{x_{2}}{\rho^{2}}\right)\Delta\rho - \Delta E_{\theta}^{p_{2}} \\ \vdots \\ \left(\frac{t\tilde{M}_{\theta_{r}}^{e_{n}}}{(\rho+x_{n})^{2}}\sum_{l=1}^{n}\sum_{\theta}^{n}-\frac{x_{n}}{\rho^{2}}\right)\Delta\rho - \Delta E_{\theta}^{p_{n}} \end{bmatrix}$$
(3)

In the framework of the EVPSC-TDT model [38–42], an individual grain (single crystal) is embedded in a HEM. The strain rate of the single crystal consists of both elastic and plastic parts: $\dot{\varepsilon}^e_{ij}$ and $\dot{\varepsilon}^p_{ij}$. For Mg alloys, the plastic deformation originates from both slip and twinning:

$$\dot{\varepsilon}_{ij} = \dot{\varepsilon}_{ij}^e + \dot{\varepsilon}_{ij}^p = M_{ijkl}^e \dot{\sigma}_{kl} + \sum_i \dot{\gamma}^\alpha P_{ij}^\alpha \tag{4}$$

where M_{ijkl}^e is the elastic compliance, $\dot{\gamma}^\alpha$ is the shear rate and $P_{ij}^\alpha = (s_i^\alpha n_j^\alpha + n_i^\alpha s_j^\alpha)/2$ is the Schmid tensor for a slip/twinning system α , with s_i^α and n_i^α being the direction and the plane normal of the slip/twinning system. The driving force for shear rate $\dot{\gamma}^\alpha$ in both slip and twinning systems is the resolved shear stress (RSS) $\tau^\alpha = \sigma_{ij} P_{ij}^\alpha$, where σ_{ij} is the Cauchy stress.

For a slip system α , the shear rate can be expressed as:

$$\dot{\gamma}^{\alpha} = \dot{\gamma}_0 \left| \frac{\tau^{\alpha}}{\tau_{cr}^{\alpha}} \right|^{\frac{1}{m}} sgn(\tau^{\alpha}) \tag{5}$$

in terms of the reference shear rate $\dot{\gamma}_0$, the critical resolved shear stress (CRSS) τ_{cr}^{α} , and the strain rate sensitivity m.

The calculation of the shear rate of twinning systems takes twin nucleation (TN) and twin growth (TG) into account. Twin nucleation (TN) is driven by the stress of the matrix. The shear rate of twining system α for TN is:

$$\dot{\gamma}_{TN}^{\alpha} = \begin{cases} \dot{\gamma}_0 \left| \frac{\tau^{\alpha}}{\tau_{cr}^{\alpha}} \right|^{1/m} & \tau^{\alpha} > 0 \\ 0 & \tau^{\alpha} \le 0 \end{cases}; \quad \dot{f}_{TN}^{\alpha} = \frac{|\dot{\gamma}_{TN}^{\alpha}|}{\gamma^{tw}}$$
 (6)

where \dot{f}_{TN}^{α} is the rate of the twin volume fraction (TVF) associated with TN, γ^{tw} is the characteristic twinning shear.

Child grains associated with newly born twins are created after TN. The growth of these child grains can be driven by the stress from both matrix and twin. As described in the TDT model, the rates of the shear strain and the TVF associated with the twin growth (TG) operation contributed from the matrix reduction (MR) and the twin propagation (TP) are:

$$\dot{\gamma}_{MR}^{\alpha} = \begin{cases} \dot{\gamma}_0 \left| \frac{\tau^{\alpha}}{\tau_{cr}^{\alpha}} \right|^{\frac{1}{m}} & \tau^{\alpha} > 0 \\ 0 & \tau^{\alpha} \le 0 \end{cases}, \quad \dot{f}_{MR}^{\alpha} = \frac{|\dot{\gamma}_{MR}^{\alpha}|}{\gamma^{tw}}$$
 (7)

$$\dot{\gamma}_{TP}^{\alpha} = \begin{cases} -\dot{\gamma}_0 \left| \frac{\tau^{\alpha}}{\tau_{cr}^{\alpha}} \right|^{\frac{1}{m}} & \tau^{\alpha} < 0 \\ 0 & \tau^{\alpha} \ge 0 \end{cases}, \quad \dot{f}_{TP}^{\alpha} = \frac{|\dot{\gamma}_{TP}^{\alpha}|}{\gamma^{tw}}$$
(8)

Correspondingly, the rates of the shear strain and the TVF associated with the de-twinning operation contributed from the matrix propagation (MP) and the twin reduction (TR) are:

$$\dot{\gamma}_{MP}^{\alpha} = \begin{cases} -\dot{\gamma}_0 \left| \frac{\tau^{\alpha}}{\tau_{cr}^{\alpha}} \right|^{\frac{1}{m}} & \tau^{\alpha} < 0 \\ 0 & \tau^{\alpha} \ge 0 \end{cases}, \quad \dot{f}_{MP}^{\alpha} = -\frac{|\dot{\gamma}_{MP}^{\alpha}|}{\gamma^{nv}}$$
(9)

$$\dot{\gamma}_{TR}^{\alpha} = \begin{cases} \dot{\gamma}_0 \left| \frac{\tau^{\alpha}}{\tau_{cr}^{\alpha}} \right|^{\frac{1}{m}} & \tau^{\alpha} > 0\\ 0 & \tau^{\alpha} \le 0 \end{cases}, \quad \dot{f}_{TR}^{\alpha} = -\frac{|\dot{\gamma}_{TR}^{\alpha}|}{\gamma^{tw}}$$
 (10)

Since the twin volume fraction (TVF) contributed from TN is marginal, the evolution of the TVF of the α^{th} twinning system, f^{α} , is primarily attributed to TG:

$$\dot{f}^{\alpha} = f^{M} \left(\dot{f}_{MR}^{\alpha} + \dot{f}_{MP}^{\alpha} \right) + f^{\alpha} \left(\dot{f}_{TP}^{\alpha} + \dot{f}_{TR}^{\alpha} \right) \tag{11}$$

where $f^M = 1 - f^{tw} = 1 - \sum_{\alpha} f^{\alpha}$ is the volume fraction of the matrix.

Twinning is terminated within a grain if the TVF f^w reaches a threshold value V^{th} , which is a function of the accumulated twin fraction V^{acc} and effective twinned fraction V^{eff} :

$$V^{th} = \min\left(1.0, A_1 + A_2 \cdot \frac{V^{eff}}{V^{acc}}\right) \tag{12}$$

where A_1 and A_2 are two governing parameters.

For slip/twinning system α , the evolution of the CRSS τ_{cr}^{α} can be expressed as:

$$\dot{\tau}_{cr}^{\alpha} = \frac{d\hat{\tau}^{\alpha}}{d\Gamma} \sum_{\beta} h^{\alpha\beta} |\dot{\gamma}^{\beta}| \tag{13}$$

Table 1 Chemical composition of extruded AZ31 alloy plate (wt%).

Al	Zn	Mn	Si	Ni	Fe	Mg
3.01	0.9	0.5	0.04	0.005	0.005	Balance

where $\Gamma = \sum_{\alpha} \int \dot{\gamma}^{\alpha} dt$ is the accumulated shear strain in the grain, and $h^{\alpha\beta}$ are the latent hardening coupling coefficients which empirically account for the obstacles on system α associated with system β . $\hat{\tau}^{\alpha}$ is the threshold stress defined by an extended Voce law [43]:

$$\hat{\tau}^{\alpha} = \tau_0^{\alpha} + \left(\tau_1^{\alpha} + h_1^{\alpha}\Gamma\right) \left(1 - \exp\left(-\frac{h_0^{\alpha}\Gamma}{\tau_1^{\alpha}}\right)\right) \tag{14}$$

Here, τ_0 , h_0 , h_1 and $\tau_0 + \tau_1$ are the initial CRSS, the initial hardening rate, the asymptotic hardening rate, and the back-extrapolated CRSS, respectively.

In the simulation of pure bending, each layer is considered as a HEM composed of plenty of grains, the strain rate \dot{E}_{ij} of which consists of elastic and plastic parts: \dot{E}^e_{ij} and \dot{E}^p_{ij} . The

strain rate is related to the stress of the HEM (Σ_{ii}) by:

$$\dot{E}_{ij} = \dot{E}_{ij}^e + \dot{E}_{ij}^p = \bar{M}_{ijkl}^e \hat{\Sigma}_{kl} + \dot{E}_{ij}^p \tag{15}$$

where \bar{M}^e_{ijkl} is the elastic compliance of the HEM, which is determined based on the Eshelby solution [44] and the self-consistent criterion. The Jaumann rate $\hat{\Sigma}$ of Cauchy stress Σ is expressed in terms of the continuum spin W:

$$\hat{\Sigma} = \dot{\Sigma} - W \cdot \Sigma + \Sigma \cdot W \tag{16}$$

With the combined approach of the discretized governing equation (Eq. (3)) and the EVPSC-TDT model (denoted as EVPSC-BEND), the mechanical behaviors of a material subjected to pure bending can be obtained. Furthermore, the bending moment on the beam is:

$$B = \int_{a}^{b} xw \Sigma_{\theta}(x) dx = t \sum_{k=1}^{n} wx_{k} \Sigma_{\theta}^{k}$$
(17)

where w is the width of the beam, t is the layer thickness, and n is the number of the discretized layers. As demonstrated in our previous work, the choice of 20 discretized layers could

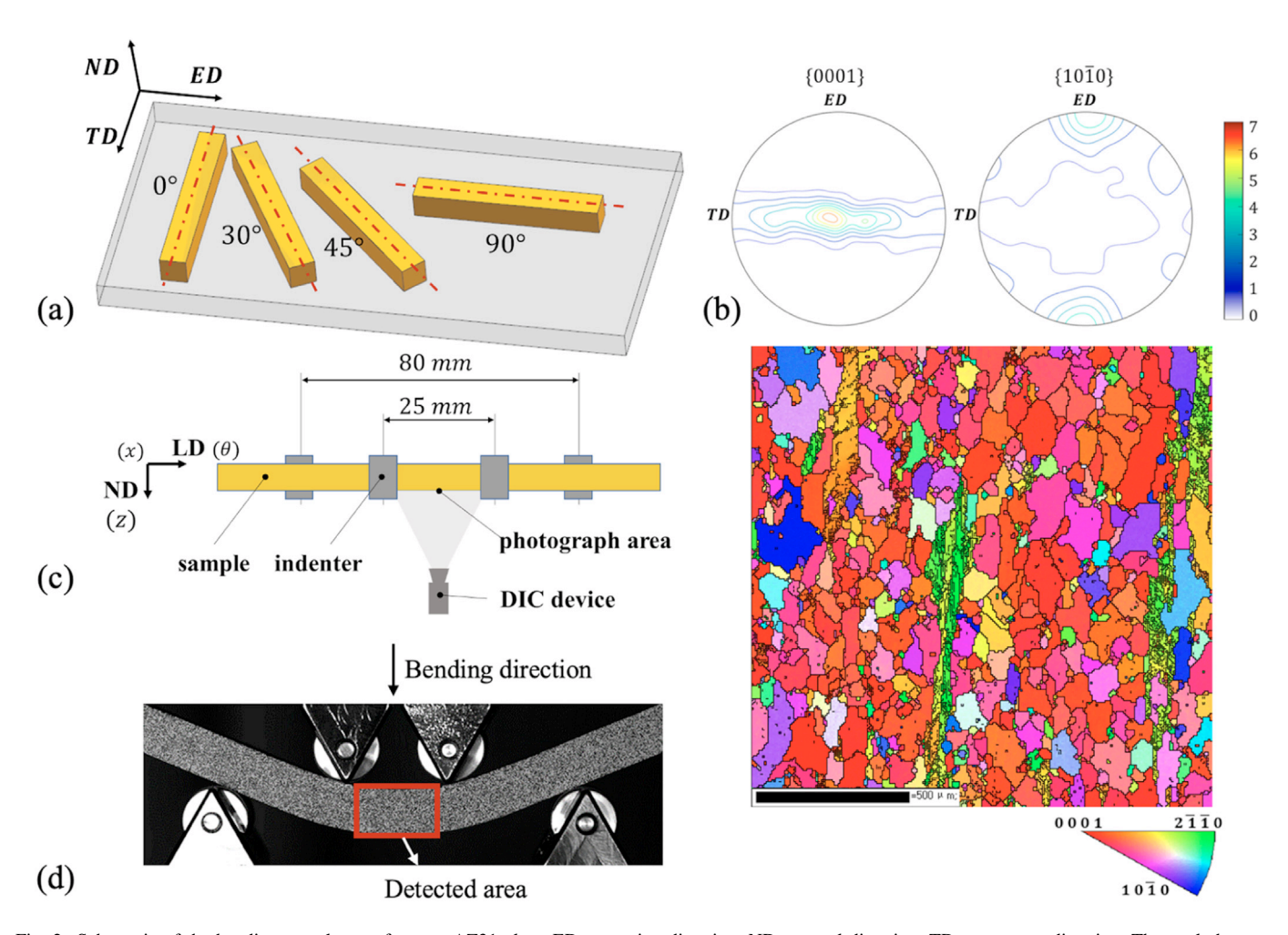


Fig. 2. Schematic of the bending samples cut from an AZ31 plate. ED: extrusion direction, ND: normal direction, TD: transverse direction. The angle between the longitudinal direction and TD is marked next to each sample. (b) Initial texture of the plate in terms of $\{0001\}$ and $\{10\overline{1}0\}$ pole figures and IPF maps. (c) The layout of the four-point bending system and DIC device. (d) A photo captured by the DIC device. (For interpretation of the references to color in this figure legend, the reader is referred to the web version of this article.)

give satisfactory results and will be employed in the current work.

3. Experimental procedure

The material employed in this work is a commercial AZ31 Mg alloy plate with an average grain size of $\sim 50 \mu m$ (Fig. 2b). The chemical composition of the extruded AZ31 alloy plate is presented in Table 1. The plate shows a typical extrusion texture with the basal poles of constituent grains perpendicular to the extrusion direction (ED) (Fig. 2b). Four bending samples with the dimension of $140 \text{ mm} \times 10 \text{ mm} \times 10 \text{ mm}$ were prepared from the plate. As shown in Fig. 2a, these samples lie within the plate and with their longitudinal directions (LDs) inclined from the transverse direction (TD) by 0°, 30°, 45°, and 90°, respectively. Fig. 2c illustrates the test system with the DIC device, where the bending test is achieved by displacing the upper two indenters with the lower two indenters remaining stationary. The distance between the lower two indenters is 80 mm and that of the upper two indenters is 25 mm. The friction between the indenter and samples has been eliminated by the 15mmdiameter rollers installed at the indenter tips. The speed of the upper two indenters is 12 ± 1 mm/min. The resultant force and the displacement of the upper indenters along the bending direction (BD) were recorded during the test. Taking advantage of the segmentation-aided digital image correlation (SA-DIC) method [45], the strain field in the speckle patterned area of the sample was detected with bending (Fig. 2d). In addition to the bending tests, the conventional tension and compression tests have been conducted on different samples at the strain rate of 5×10^{-4} /s.

4. Results and discussion

4.1. Parameter calibration

Slip systems including basal $\langle a \rangle (\{0001\} \langle 11\overline{2}0 \rangle)$, prismatic $< a > (\{10\bar{1}0\} < 11\bar{2}0 >)$ and pyramidal < c + a > $(\{\overline{11}22\} < \overline{11}23 >)$, and extension twin system $\{10\overline{12}\} <$ 1011 > that accommodate the plastic deformation have been included in the EVPSC-BEND model. At room temperature, the selected four mechanisms dominate the deformation [46], while others only have a minor effect on the deformation behaviors. This work's selection has been widely accepted by many researchers in their practice in Mg alloys [7,42,47,48]. The elastic constants at room temperature of the magnesium alloy are taken from Simmons et al. [49]: $C_{11} = 58.0$, $C_{12} = 25.0$, $C_{13} = 20.8$, $C_{33} = 61.2$ and $C_{44} = 16.6$ (GPa). The reference slip/twinning rate $\dot{\gamma}_0$ and the rate sensitivity m are prescribed to be the same for all slip/twinning systems: $\dot{\gamma}_0 = 0.001 \text{ s}^{-1}$ and m = 0.05, respectively. The hardening parameters of these deformation mechanisms have been determined by fitting both the tensile and compressive stress-strain curves of the 90° sample. As shown in Fig. 3, the simulated results match well with the corresponding experiments. The inset in Fig. 3 is the initial texture of the sample in terms of

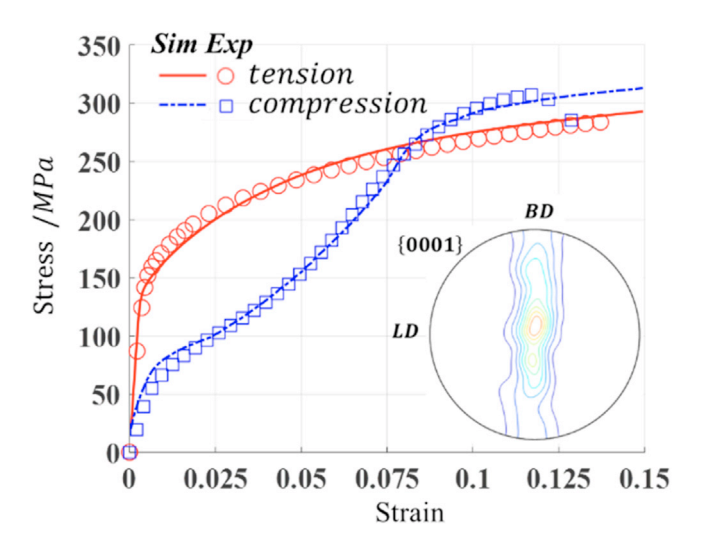


Fig. 3. The stress-strain curves of experiment and simulation for uniaxial tension and uniaxial compression of 90° sample. The circle and square markers denote the experiment data.

the {0001} pole figure, where LD is the loading direction of the uniaxial tests. The determined parameters associated with the EVPSC-BEND model are listed in Table 2. Without otherwise mentioned, the determined hardening parameters are used in all subsequent simulations.

The measured stress-strain curves of 0°, 30°, and 45° samples under tension and compression are presented in Fig. 4. The initial textures of these samples, which rotate from the initial texture of the 90° sample only by the corresponding inclination angle, are also included as insets. These tests have been simulated in parallel by the EVPSC-BEND model with the numerical results in good consistency with the experiments (Fig. 4). Referring to the counterparts of the 90° sample (in gray), both the experimental and numerical stressstrain curves have a strong dependency on the initial textures. This dependency can be observed from the different tensioncompression asymmetry and the magnitude of the flow stress. The relative activities of various deformation mechanisms under different loading cases are shown in Fig. 5. The deformation twinning is generally more active under compression than tension. Therefore, the stress-strain curve shapes towards "S" under compression and towards "C" under tension. Moreover, in the cases of tension, the twinning activity decreases with increasing the inclination angle, while this trend is the opposite in the cases of compression. Therefore, the "S-shape" of the compressive stress-strain curve becomes more obvious with increasing the inclination angle. Among different samples, the twinning activities under tension and compression are close to each other for the 0° sample. Therefore, among the samples investigated, the samples with the mildest and strongest tension-compression asymmetry are the 0° and 90° samples, respectively.

4.2. Texture-dependent bending behaviors

The force (F) and displacement are directly measured in the four-point bending tests, which are transferred to the bend-

Table 2 List of values of the hardening parameters involved in the EVPSC-TDT model. $h^{\alpha\beta}$ represents the latent hardening coefficients of slip systems associated with the extensive twin systems.

Mode	$ au_0(ext{MPa})$	$\tau_1(MPa)$	$h_0(MPa)$	h ₁ (MPa)	$h^{lphaeta}$	A_1	A_2
Basal	2	27	389	35	2	NA	NA
Prismatic	68	44	459	25	1	NA	NA
Pyramidal	92	82	878	20	1	NA	NA
Extensive twin	12	0	0	0	1	0.4	0.65

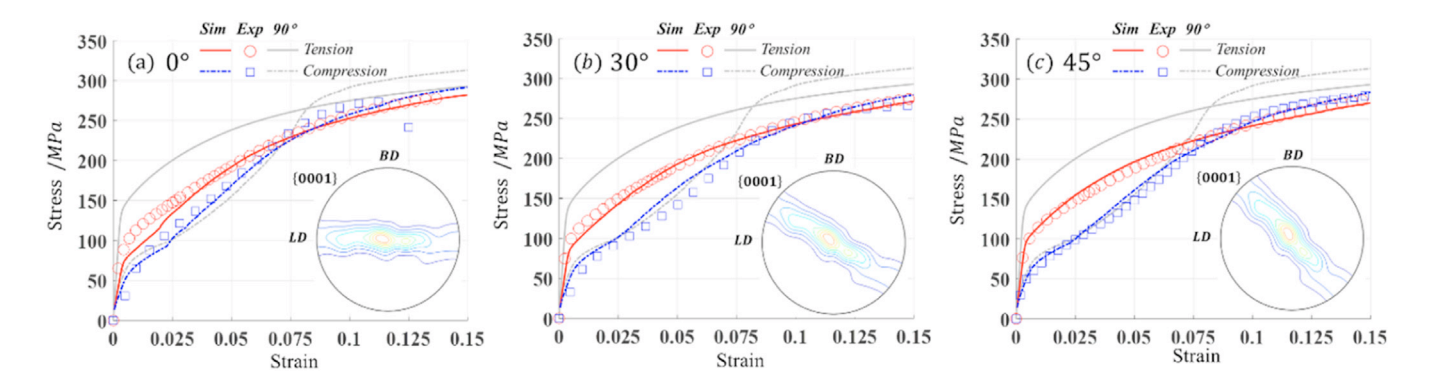


Fig. 4. The stress-strain curves of experiment and simulation for uniaxial tension and uniaxial compression of 0°, 30°, and 45° samples. The circle and square markers denote the experiment data.

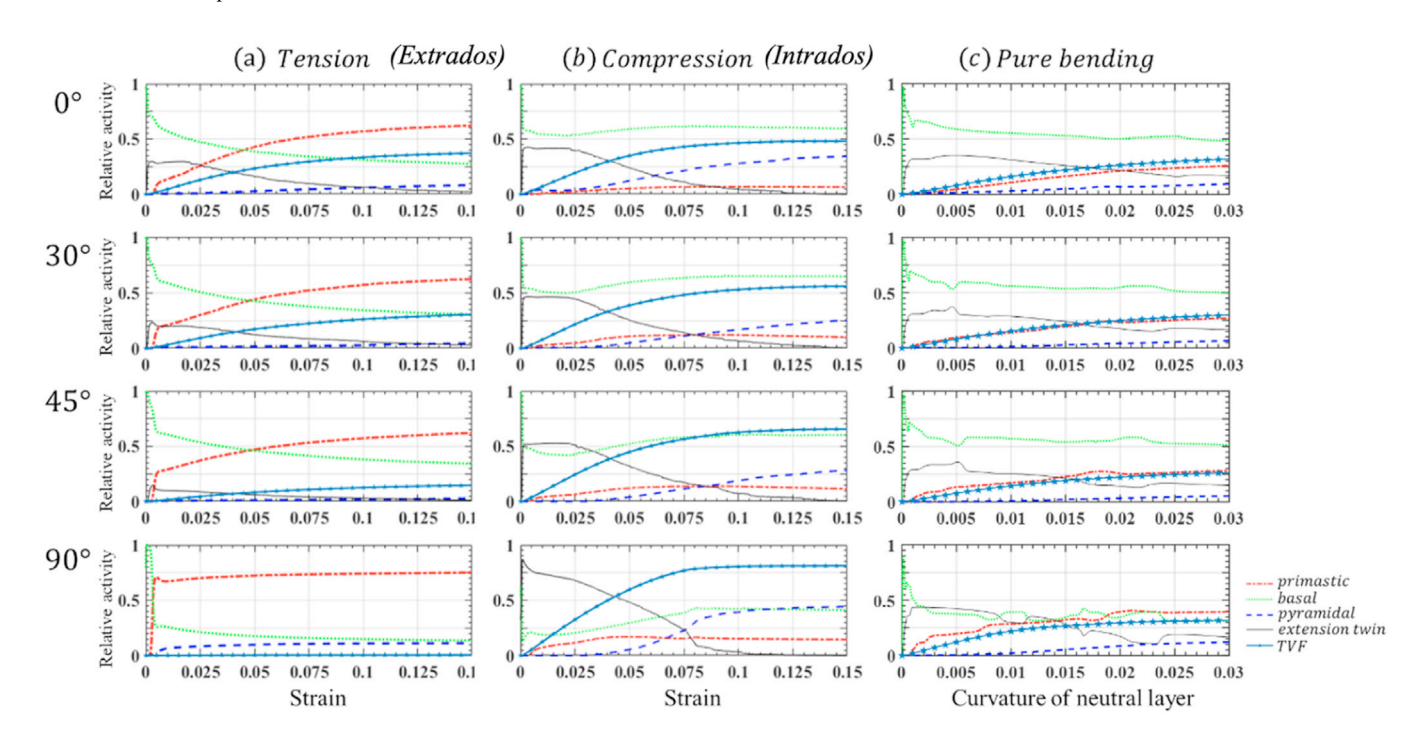


Fig. 5. Relative activities of various deformation mechanisms in Mg alloy under (a) tension, (b) compression, and (c) bending-

ing moment (B) and the curvature $(1/\rho)$ with the aid of the DIC device and the recorded geometry of the sample. The transformation approach was adopted from the previous work of Tang et al. [37]. Besides, the four-point bending tests of various samples have been simulated by the EVPSC-BEND model utilizing the parameters listed in Table 2. Fig. 6 shows the obtained responses of the bending moment (B) to the curvature $(1/\rho)$ in these bending tests, where the measure-

ments and simulations are in good agreement. The relative errors between them are small with values of 6.04%, 5.06%, 3.36%, and 7.00% for 0°, 30°, 45°, and 90° samples, respectively. Compared to the uniaxial tension and compression tests (Figs. 3 and 4), the deviation among the moment-curvature curves associated with different samples is drastically decreased. This is because the bending behavior is an integrated response of both tension and compression, which alleviates

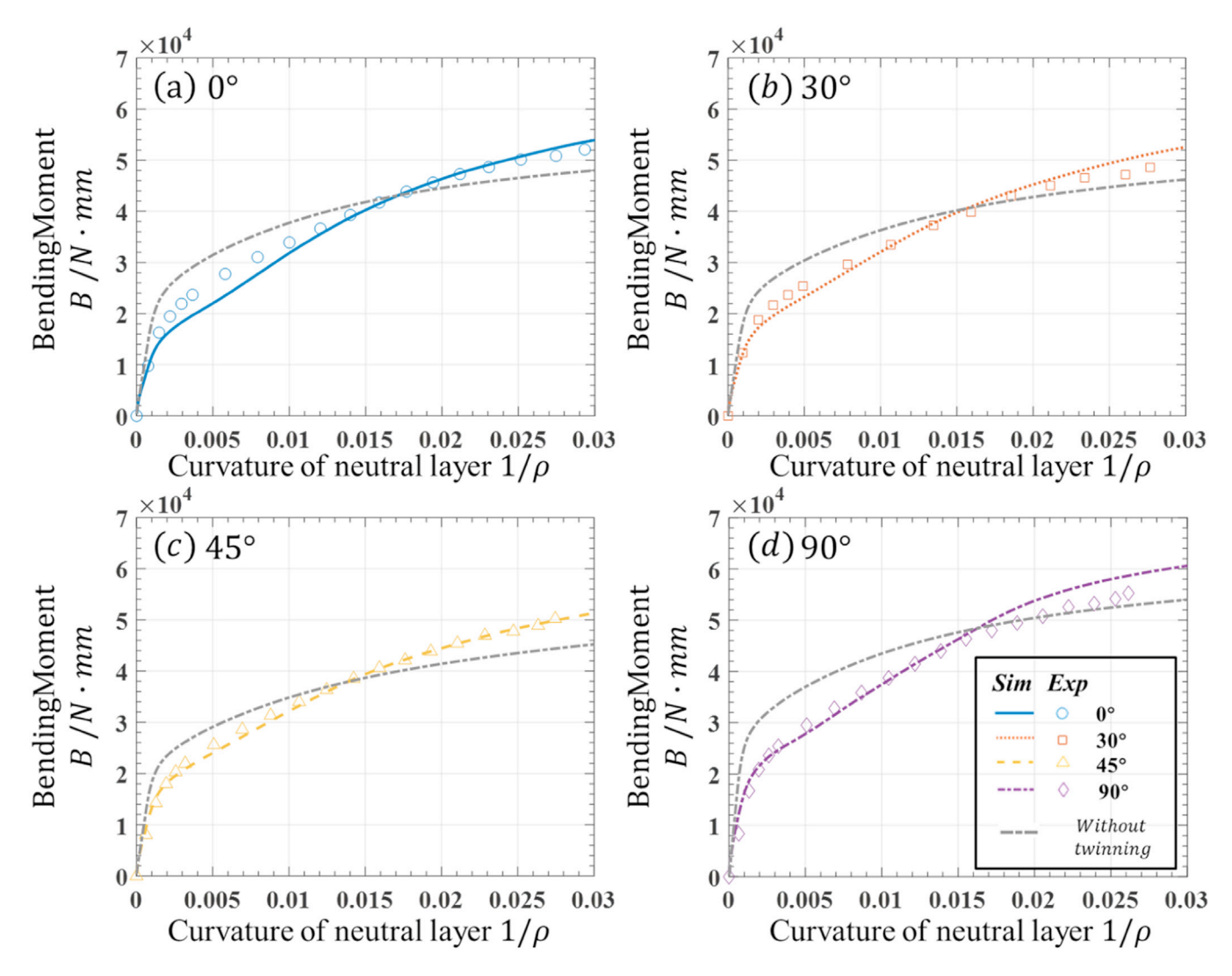


Fig. 6. Measured (symbols) and predicted (lines) moment-curvature curves of 0° , 30° , 45° , and 90° samples under four-point bending. The predicted results without deformation twinning are also included (gray lines). (For interpretation of the references to color in this figure legend, the reader is referred to the web version of this article.)

texture dependence in terms of bending-curvature curves. The activities of the various deformation mechanisms associated with bending are approximated through averaging the corresponding activities over all layers (Fig. 5c). These activities of various samples are close to each other under bending. There has been a gradual rise in the activity of prismatic since the inclination angle increases. Turning now to the activity of twinning, it decays more slowly in bending than in tension or compression, because the twinning saturated gradually from the outside layers to the central layer. However, the differences among the moment-curvature curves are still noticeable. The bending moment of 90° sample is the largest, which is not surprising considering that the 90° sample exhibits the highest strength of tension and compression among them. When the curvature is beyond 0.015, the order of moment (B) is 90° , 0° , 45° , and 30° samples.

To evaluate the role of deformation twinning, a set of simulation cases with the twinning mechanism excluded are con-

ducted by the EVPSC-BEND model. The obtained results are included as gray lines in Fig. 6, where the characteristic S-shape of the moment-curvature curves cannot be captured by the model anymore. Moreover, overestimation and underestimation on the bending moments are obvious before and after the curvature of 0.015, respectively. These results manifest that deformation twinning is responsible for the typical bending behaviors of Mg alloys and the importance of including accurate twinning scheme in modeling.

Because of the bending nature, the bending moment is a collective response of both tensile and compressive regions, which results in a weak dependency on the initial texture of the Mg alloys. Alternatively, the shifting of the neutral layer, resulting from the tension-compression asymmetry, should be a good indicator to demonstrate the texture dependency. Fig. 7 presents the shifting of the neutral layer in terms of the displacement of the neutral layer from the geometrical central layer (GCL). A negative displacement indicates the

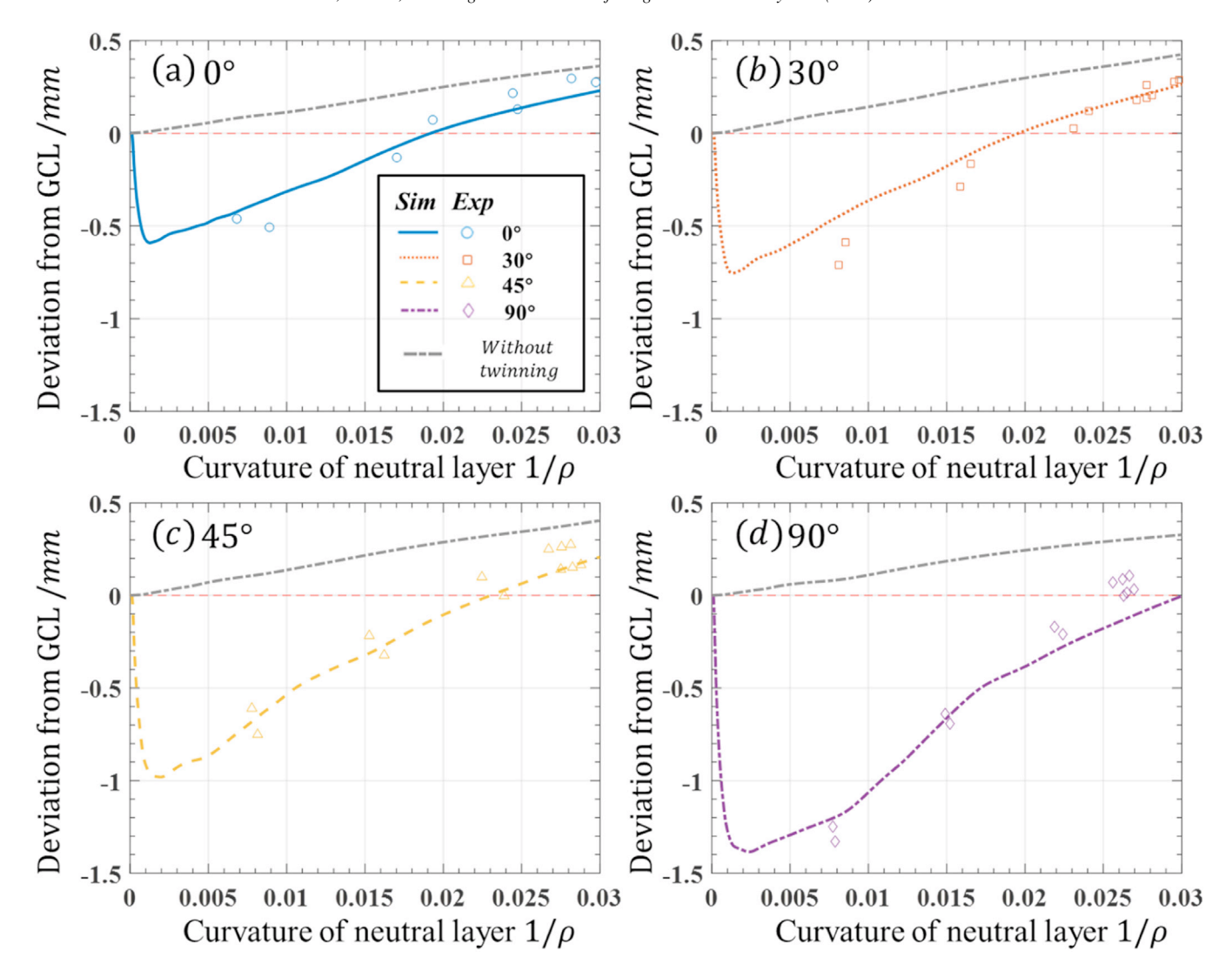


Fig. 7. Displacement of the neutral layer as a function of the curvature 1/ρ from the EVPSC-BEND model and DIC measurements.

neutral layer shifts towards the extrados. The scattered symbols are from the DIC measurements, showing the consistency between the predicted movement of the neutral layer and the experimental results. The neutral layer firstly shifts towards the extrados and then back to GCL in all samples. The shifting extremes and the corresponding curvatures of the neutral layer vary with samples. The predicted maximum neutral layer shifting displacements of 0°, 30°, 45°, and 90° samples are 0.59, 0.75, 0.98, and 1.38 mm at the curvatures of 0.019, 0.020, 0.023 and 0.029 (unit of 1 mm), respectively. The compressive stress is initially lower than, but eventually surpasses, the tensile one for all samples, as shown in Figs. 3 and 4. The neutral layer shifting relies on this twin-induced strong tension-compression asymmetry of each sample. To further prove this, auxiliary calculations with twinning excluded are conducted and with results presented as gray curves in Fig. 7. Apparently, the neutral layer shifts monotonically towards the intrados in all samples, and its difference among 0° , 30°, 45°, and 90° samples becomes relatively less significant.

Fig. 8 shows the measured and predicted strain distributions at the bending displacement (i.e., the displacement of upper indenters) of 5 and 20 mm. The primary strain component E_{θ} distributes linearly along with the thickness, while the other two components E_r and E_z distribute with obvious non-linearity. This phenomenon is clearly revealed from both the measurements and simulations. In addition, the corresponding stress distributions at the bending displacement of 5 and 20 mm are displayed in Fig. 9, which are intricately measured via experiment but feasible through the model. At the bending displacement of 5 mm, the stress component Σ_r is nearly zero and the shapes of the stress distribution of Σ_{θ} in compressive and tensile zones are similar to those of compressive and tensile stress-strain curves shown in Figs. 3 and 4. With increasing the bending displacement, the stress component Σ_r becomes as high as 20 MPa. To satisfy the force balance of zero circumferential force, the shaded areas in the tensile and compressive regions have to equal to each other, which demands the shifting of the neu-

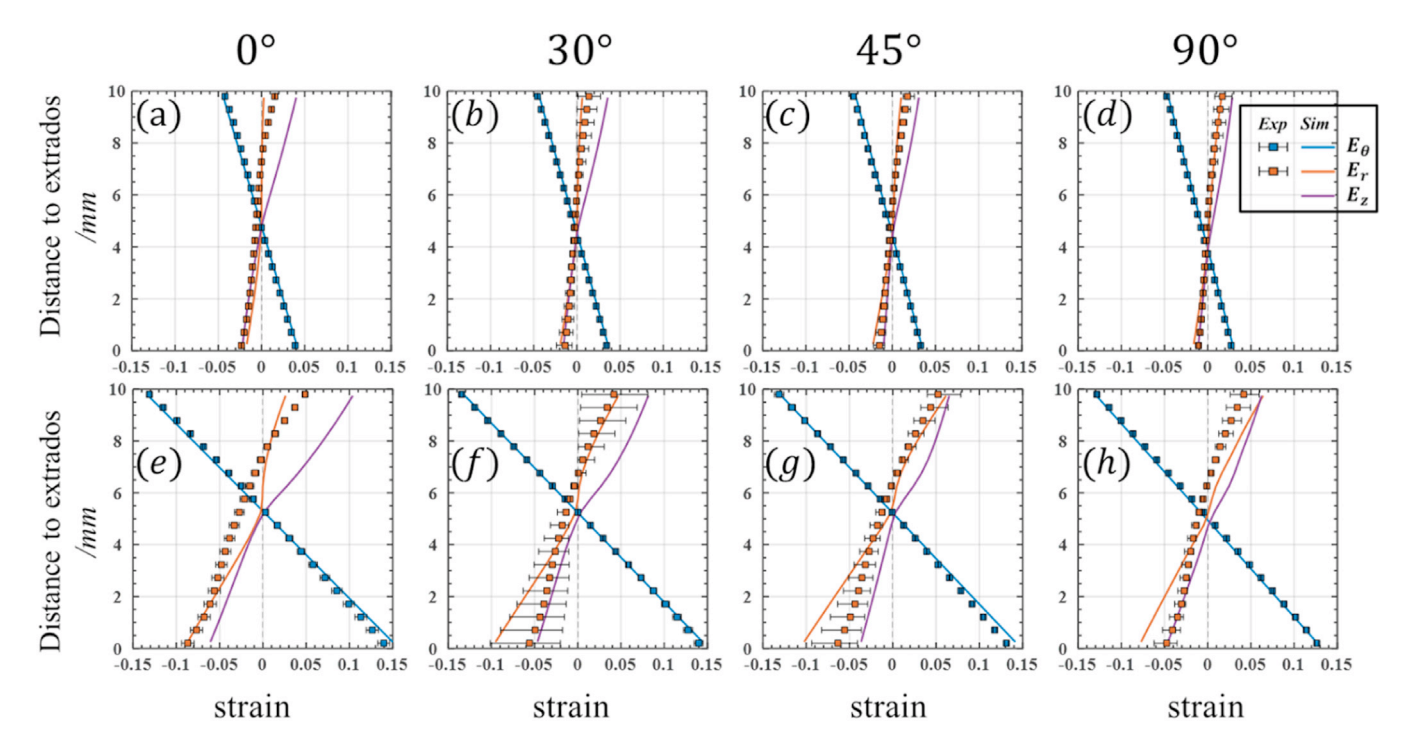


Fig. 8. The strain distribution within the 0°, 30°, 45°, and 90° samples at bending displacements of (a~d) 5 mm and (e~h) 20 mm.

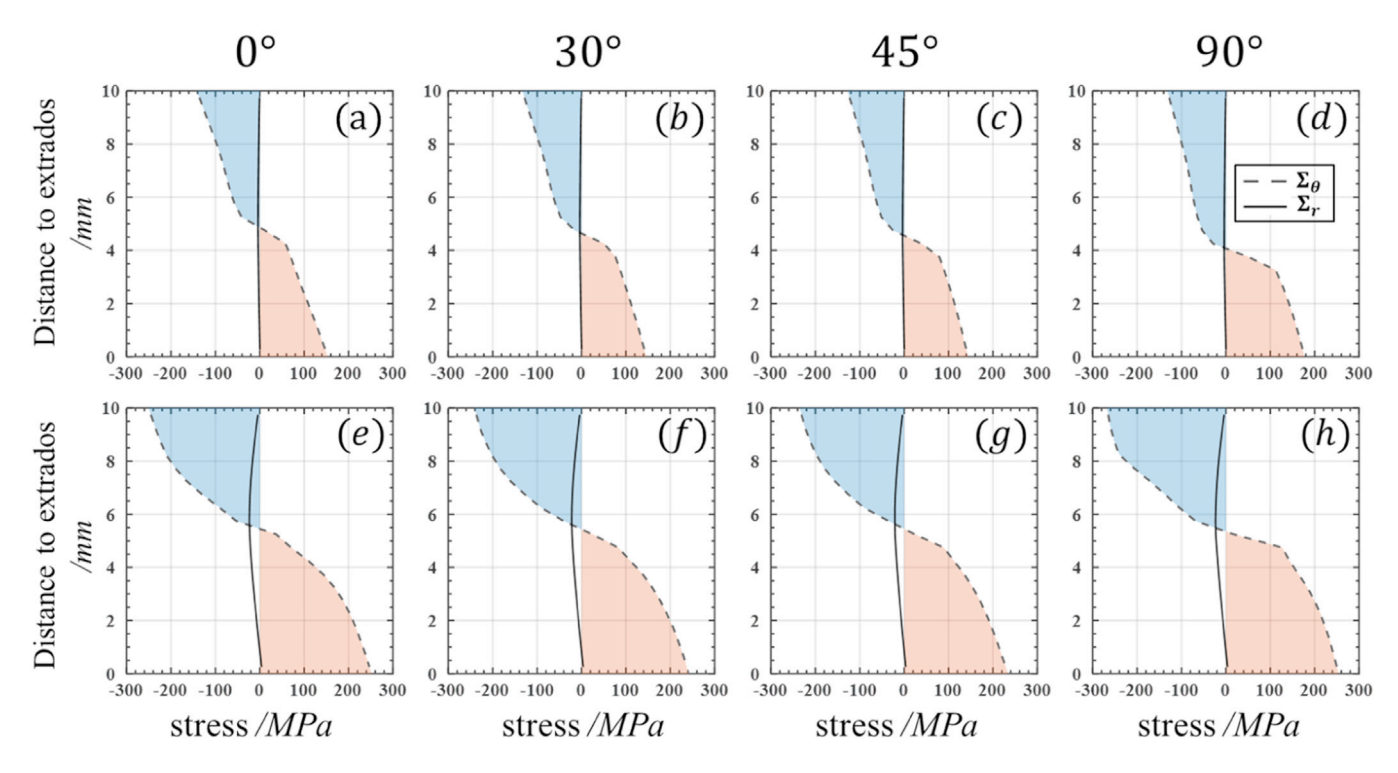


Fig. 9. The stress distribution of 0°, 30°, 45°, and 90° samples at bending displacement of 5 mm (a~d) and 20 mm (e~h).

tral layer. Taking the 90° sample as an example, the neutral layer (position with zero Σ_{θ}) evolves to above the GCL at the bending displacement of 20 mm, while it is below the GCL at the bending displacement of 5 mm. Though less obvious than the 90° sample, similar distribution of the stress components and resulted shifting of the neutral layer are ob-

served for other samples. In summary, the dependence of the bending behavior on the initial texture results from the different distributions of the stress and strain within the beam samples, which is ascribed to the different activities of deformation mechanisms, especially deformation twinning, of Mg alloys.

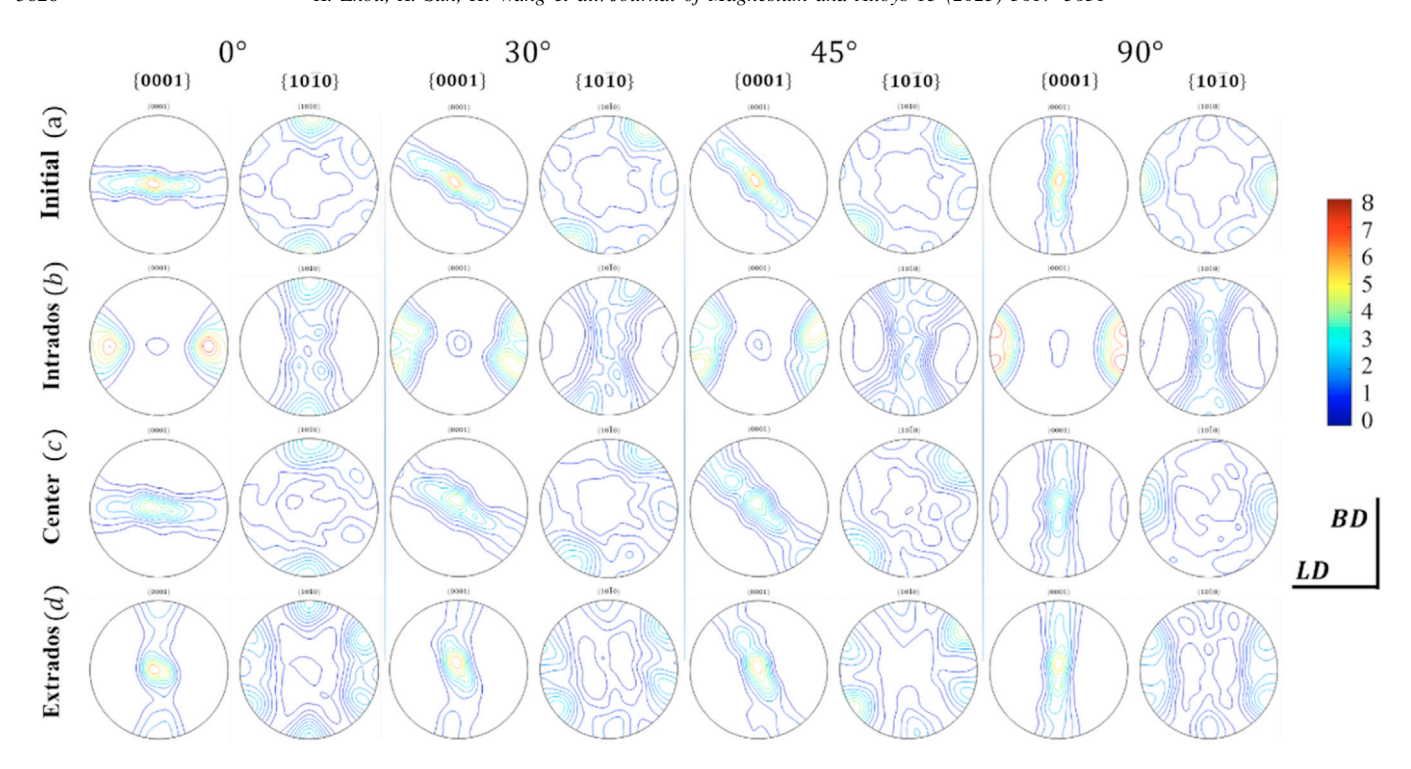


Fig. 10. Initial and deformation textures of 0°, 30°, 45°, and 90° samples at intrados, center, and extrados at the curvature of 0.03.

4.3. Texture evolution in the bending process

The initial texture, inherited from the previous forming process of extrusion, distributes nearly even within the beam samples before the bending tests (Fig. 10a). Because of the inhomogeneous nature of bending, the texture is supposed to evolve differently at different locations. As demonstrated in Appendix, the EVPSC-BEND model reproduces well the measured deformation textures at different locations of the beam. Therefore, the texture evolution was also tracked and outputted in the simulations. The deformation textures at the curvature of 0.03 at the intrados, center, and extrados are presented in Fig. 10 in terms of {0001} and {1010} pole figures. The conspicuous twinning textures with nearly 90° rotation of the grain orientation appeared at the intrados of all samples (the second row), which is further confirmed by the drastic TVF evolution in Fig. 11. Conversely, the twinning texture in extrados becomes less and less noticeable with the inclination angle until it almost disappears in the 90° sample. The reason behind this phenomenon is the polar nature of twin that can only be activated unidirectionally. Under bending, either the compressive stress at intrados or the tensile stress at extrados are both parallel to the longitudinal direction of the samples. If a sample has more grains oriented initially with basal poles perpendicular to the LD, the texture at intrados will change drastically because of the abrupt orientation change by twinning. Therefore, the texture evolves at the intrados more obviously in the 90° sample than in other samples. In contrast, the texture evolves the most drastically at the extrados in the 0° sample, where the basal poles of grains are oriented preferentially parallel to LD.

For the center layer, the magnitude of the stress and strain are much less than those of the two surface layers. Therefore, the deformation textures at the center layer retain mainly the initial textures (Fig. 10c). However, instead of a uniaxial stress state, the center layer is subjected to a multiaxial stress state (Fig. 12). Therefore, as shown in Fig. 12, activities of various deformation mechanisms also distinct from those shown in Fig. 5. At a certain curvature, the farther the neutral layer moved towards extrados, the more active the twinning mechanism and TVF are. Moreover, the center layer experiences a compressive Σ_{θ} first, then to a tensile one with bending. Such a stress state change results in detwinning in the center layer, which is clearly reflected in the TVF in Fig. 11d. This unique feature hardly occurs in other monotonic loading cases of tension, compression, torsion, etc.

4.4. Twin distribution within the beams

The distributions of the developed TVF in 0° , 30° , 45° , and 90° samples are compared in Fig. 13. At the displacement of 5 mm, the twinning is not saturated yet at either intrados or extrados and thus distributes linearly on both tensile and compressive halves. When the displacement reaches 20 mm, the TVF ranges from ~ 50 to $\sim 80\%$ around the intrados, while it ranges from 0% to 40% around the extrados. Gradient twin structures have been constructed by bending in different samples with different bending displacements. Plentiful twins in one half of the beam and rare twins in the other half can be observed in the 90° sample. Comparable twin structures in both halves are constructed in the 0° sample. As demonstrated in previous work, the property of material could be

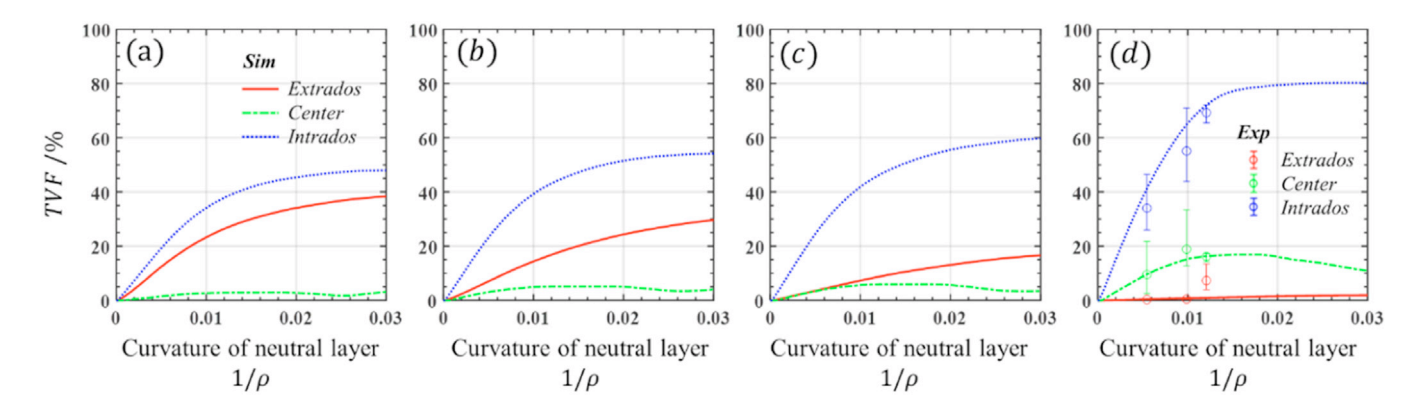


Fig. 11. The evolution of predicted TVF in the three layers of (a-d) 0° , 30° , 45° , and 90° samples under bending, respectively. And the experimental data in (d) were obtained from Tang et al. [37]. (For interpretation of the references to color in this figure legend, the reader is referred to the web version of this article.)

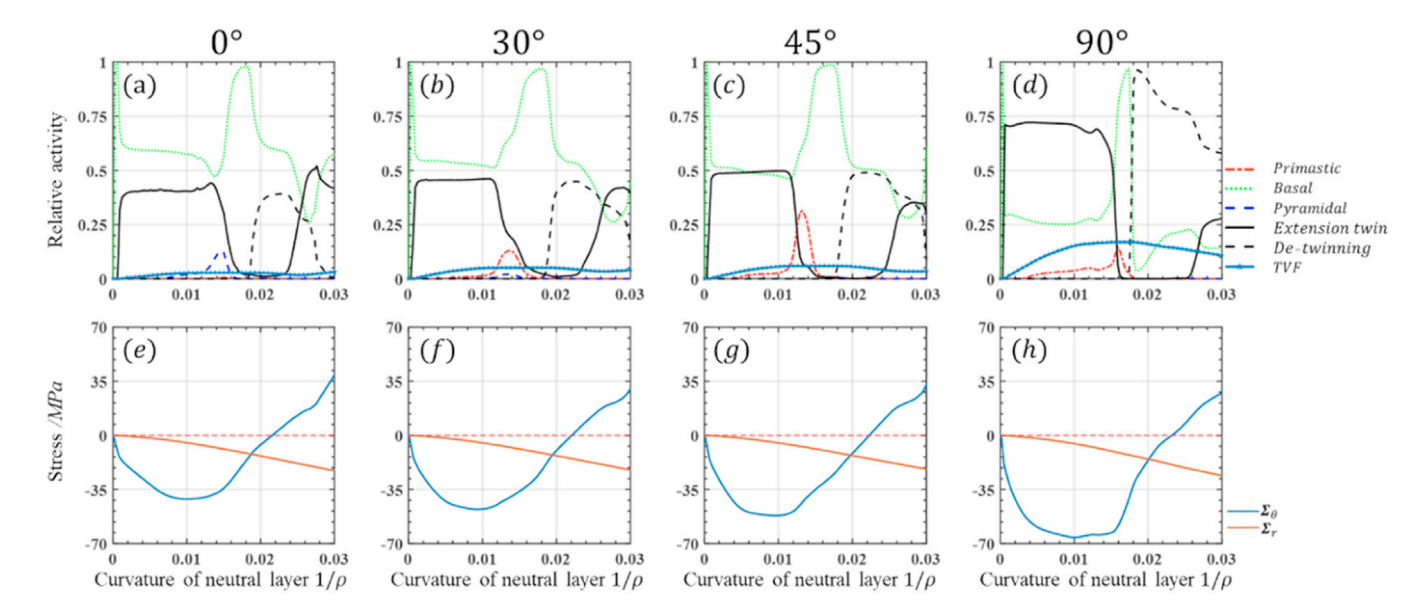


Fig. 12. The relative activities of various deformation mechanisms (a-d) and the stress components Σ_{θ} and Σ_{r} (e-h) in the center layer of 0°, 30°, 45°, and 90° samples under bending, respectively.

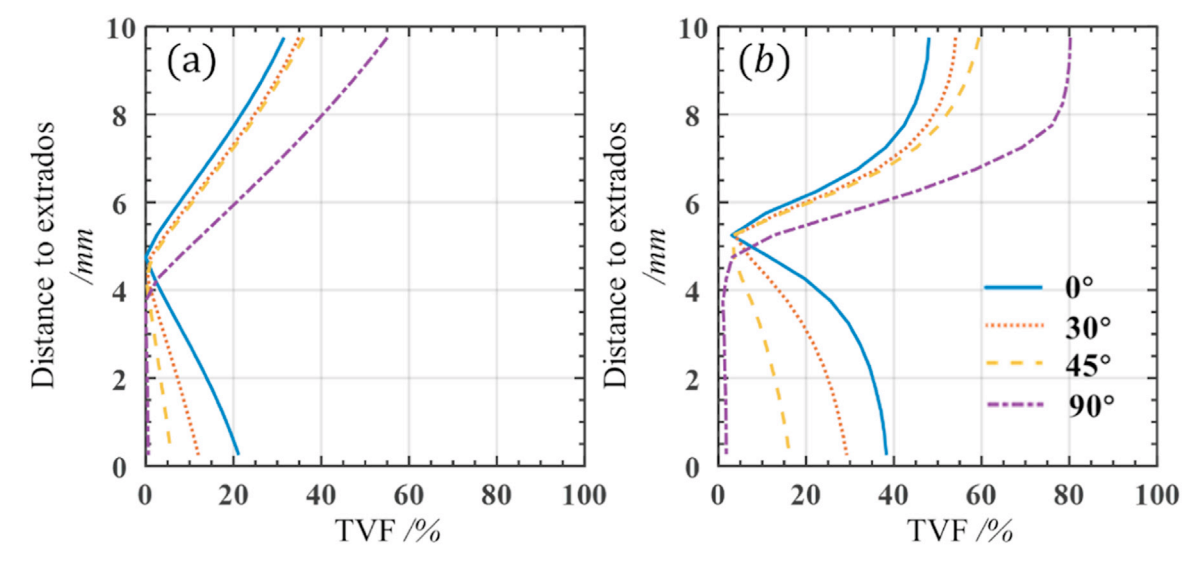


Fig. 13. The distribution of the TVF along the height direction of the samples at the displacement of (a) 5 mm and (b) 20 mm.

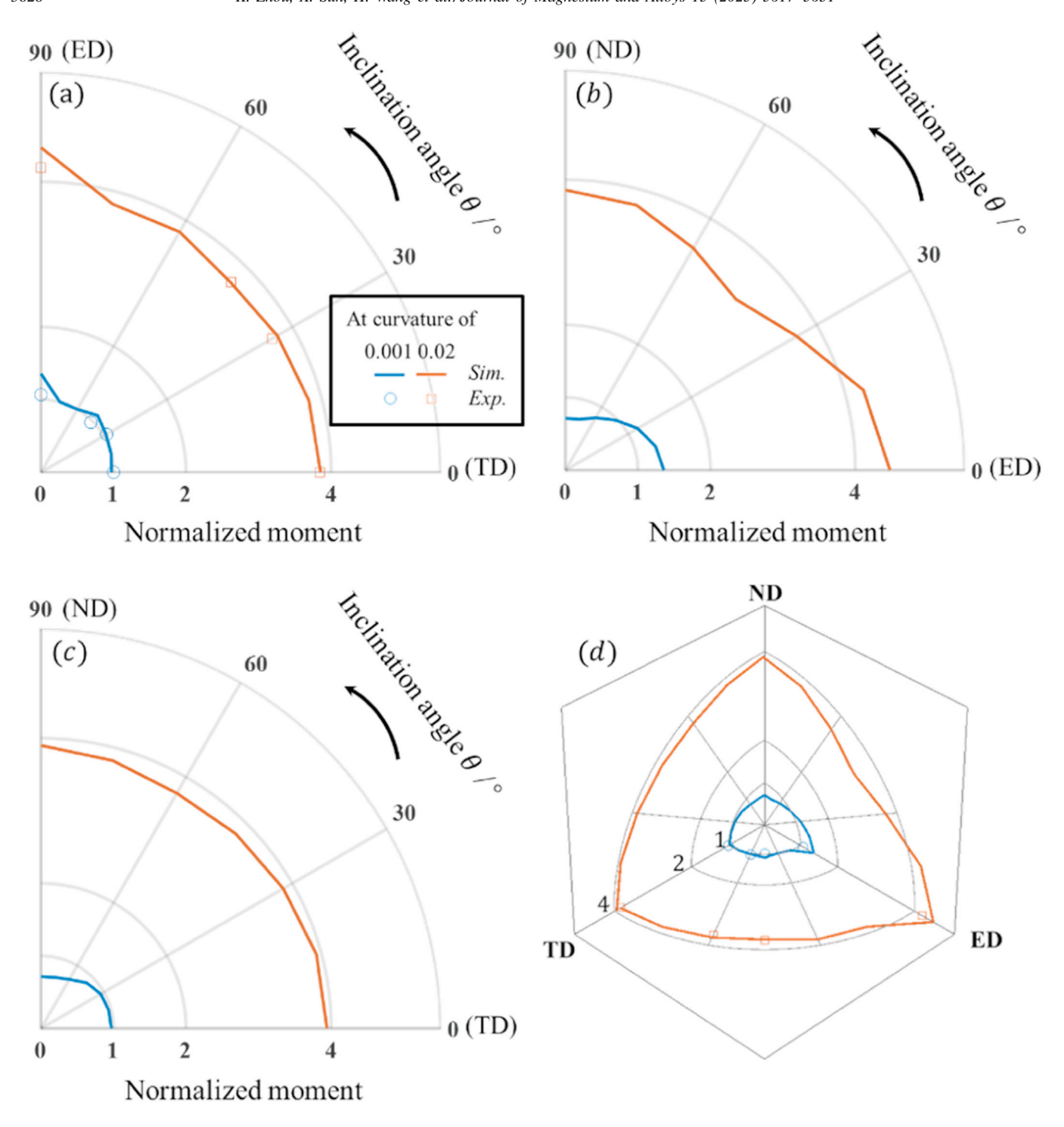


Fig. 14. The moment-angle curves at the curvature of 0.001 and 0.2 in the polar coordinate: (a) samples with LD from TD (inclination angle = 0) to ED; (b) samples with LD from TD to ED; (c) samples with LD from TD to ND; (d) the 3D views of the above moment-angle curves.

enhanced significantly with gradient microstructure [50]. The current work illustrates that a variety of gradient twin structures could be achieved through bending. This is of particular significance as it offers an efficient and economical processing method to enhance the mechanical properties of not only hcp Mg alloys [51] but also other materials where deformation twinning can be induced [52–54].

4.5. Moment-inclination angle relation

In order to intuitively show the texture-dependent bending behaviors of Mg alloys, the moment-inclination angle relation at the curvatures of 0.001 and 0.2 are shown in Fig. 14. The polar angle is the inclination angle between the LD and one specific direction in sample axes. For example, in Fig. 14a, the

LD is oriented from TD (0°) to ED (90°) , and the width direction of all samples is retained as ND. The bending moments are normalized by the experimental moment of 0° sample at the curvature of 0.001, which corresponds to the apparent yielding under bending (see Fig. 6). In a similar fashion, additional simulations on samples inclined within the ED-ND and TD-ND planes are conducted. Fig. 14 shows the normalized moment-angle curves in the TD-ED plane, ED-ND plane, and TD-ND plane of the plate. As shown in Fig. 14a, at the curvature of 0.001, both the experimental and simulated results are around 1, indicating a weak texture dependence. The texturedependent bending behavior in the ED-ND plane (Fig. 14b) is the most obvious, especially for the initial yielding moment, where the bending moment ratio varies from 1.385 to 0.743. Fig. 14b and c both indicate a decreasing tendency of the yield moment when the LD is oriented towards ND. The texture-dependence retains similar with increasing the bending curvature. At the curvature of 0.02, a weak texture dependence is observed within the TD-ED plane and TD-ND plane with the normalized moment approximately equal to 4. In contrast, the bending moments do not vary monotonically with increasing the inclination angle in the ED-ND plane. As shown in Fig. 14d, within the three planes investigated, the ED-sample bears the largest moment at the curvature of 0.001, while the ND-sample bears the smallest. With further bending, though the ED-sample still bears the largest moment, the one that bears the least moment changes to the sample inclined 45° from the ED within the ED-ND plane. Therefore, the dependence of the bending behavior on the texture also evolves with the loading history.

5. Conclusions

The crystal plasticity-based bending-specific approach EVPSC-BEND has been applied to uncover the texture-dependent bending behavior of the Mg alloy. Samples with different initial textures prepared from the extruded AZ31 plate and have been undergone the four-point bending process. DIC technique has been used to capture the strain field of pure bending. Based on both the experimental and simulated results, the following conclusions can be drawn:

- (1) The experimental results reveal that the bending behaviors of the extruded AZ31 plate depend strongly on the sample orientation, i.e., the initial texture. The maximum neutral layer shifting displacements increase as the inclination angle increases. The sample with LD orienting to ED, bears the largest moment. And the distribution of the internal strains changes with initial texture altering. All these phenomena are largely attributed to the twinning activity.
- (2) The EVPSC-BEND model accurately simulates deformation mechanisms and reproduces the behavior of samples with different initial textures. Especially, the model provides full-field stress distribution and information on various deformation mechanisms that are difficult to obtain experimentally.

- (3) The texture-dependent bending behavior of Mg alloys is caused by differences in deformation mechanism activity, with twinning playing a key role other than the slips. Excluding twinning from the simulation weakens the texture-dependent behavior, such as the shifting of the neutral layer. The twin volume fraction's development and evolution at different locations in different beam samples further support this role.
- (4) The distribution of the TVF within the Mg alloy beam sample oriented along the extrusion direction was captured by the EVPSC-BEND model and confirmed from the experimental results. In addition, very different distributions of the TVF are obtained in different beam samples with different bending displacements. This result inspires the gradient twin structures design through bending on Mg alloys to achieve desired mechanical properties.
- (5) Numerical bending tests have been conducted on samples virtually prepared with different inclination angles within TD-ND and ED-ND planes. The moment-inclination angle relation presented in the polar coordinate provides a complete picture of the texture-dependency on the bending behaviors of Mg alloys, which is invaluable in the manufacturing and application of Mg alloys.

Declaration of competing interest

The authors declare that they have no known competing financial interests or personal relationships that could have appeared to influence the work reported in this paper.

Acknowledgments

This work was supported by State Key Laboratory for GeoMechanics and Deep Underground Engineering, China University of Mining & Technology, Beijing (XD2021021), and the National Natural Science Foundation of China (Nos. 52075325, 51975365, and 52011540403).

Appendix

The prediction of the EVPSC-BEND model on the deformation textures is confirmed by the experimental results (after Tang et al. [37]). The experimental and predicted textures in terms of $\{0001\}$ and $\{10\overline{1}0\}$ pole figures are compared in Fig. A1. The quality of the texture prediction is assessed by the texture difference parameter (TDP), defined by

$$TDP = \frac{\sum_{iG} |VF_1(iG) - VF_2(iG)|}{\sum_{iG} (VF_1(iG) + VF_2(iG))}$$
(A1)

where $VF_1(iG)$ and $VF_2(iG)$ are the volume fractions of the grains falling in the discretized grid iG for two textures under comparison. The EVPSC-BEND model captures well the developed textures as the TDPs are 0.07180 at the intrados, 0.06563 at the center, and 0.11894 at the extrados.

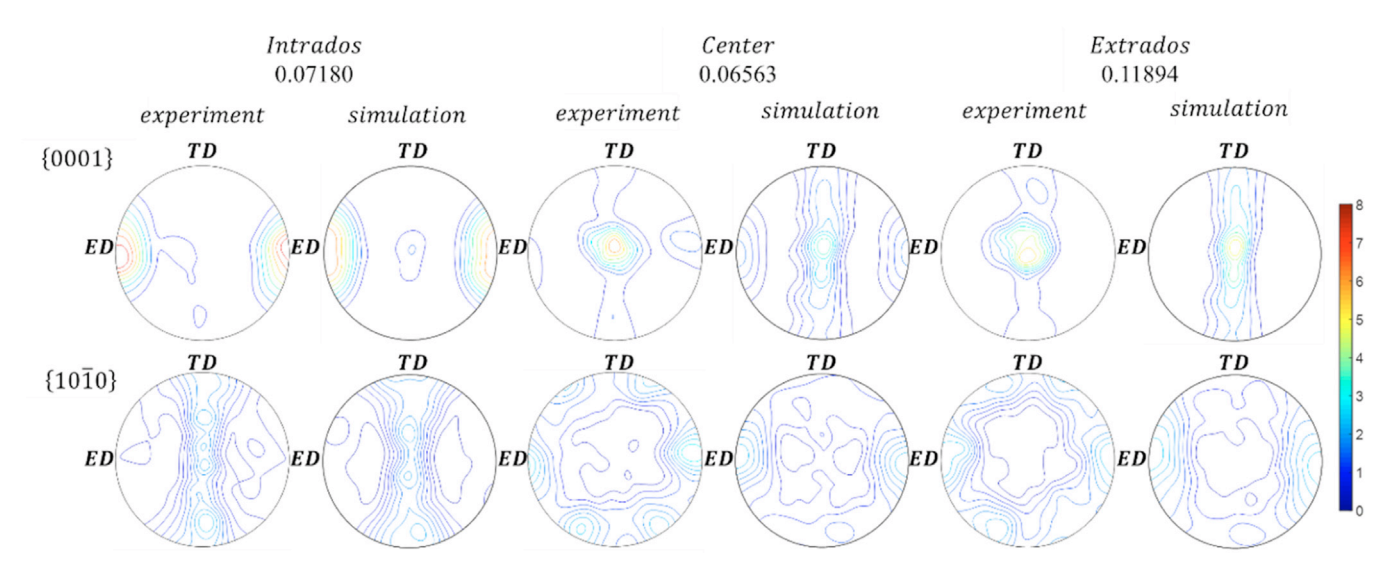


Fig. A1. Measured and predicted textures at intrados, center, and extrados layers of the sample along ED (90° sample) at the curvature of 0.012.

References

- [1] D. Eliezer, E. Aghion, F.H. Froes, Adv. Perform. Mater. 5 (1998) 201– 212, doi:10.1023/A:1008682415141.
- [2] S.R. Agnew, J.F. Nie, Scr. Mater. 63 (2010) 671–673, doi:10.1016/j. scriptamat.2010.06.029.
- [3] T.M. Pollock, Science 328 (2010) 986–987 (1979), doi:10.1126/science. 1182848.
- [4] Y. Yang, X. Xiong, J. Chen, X. Peng, D. Chen, F. Pan, J. Magn. Alloy. 9 (2021) 705–747, doi:10.1016/j.jma.2021.04.001.
- [5] C.M. Cepeda-Jiménez, M.T. Pérez-Prado, Acta Mater. 108 (2016) 304–316, doi:10.1016/j.actamat.2016.02.023.
- [6] Y.B. Chun, C.H.J. Davies, Scr. Mater. 64 (2011) 958–961, doi:10.1016/j.scriptamat.2011.01.044.
- [7] H. Qiao, X.Q. Guo, A.L. Oppedal, H. El Kadiri, P.D. Wu, S.R. Agnew, Mater. Sci. Eng. A 687 (2017) 17–27, doi:10.1016/j.msea.2016.12.123.
- [8] B. Shi, C. Yang, Y. Peng, F. Zhang, F. Pan, J. Magn. Alloy. 10 (2022) 1476–1510, doi:10.1016/j.jma.2022.03.006.
- [9] C.S. Roberts, Magnesium and Its Alloys, John Wiley & Sons, Inc., New York, 1960.
- [10] F.E. Hauser, P.R. Landon, J.E. Dorn, Trans. Am. Soc. Met. 48 (1956) 986–1002.
- [11] E.C. Burke, W.R. Hibbard, JOM 4 (1952) 295–303, doi:10.1007/
- [12] R.E. Reed-Hill, W.D. Robertson, Trans. TMS AIME 212 (1958) 256–259 https://www.scopus.com/inward/record.uri?eid&2-s2.0-00120 82515&partnerID=40&md5=004337de592788f6f95e5e0b37cb87c6.
- [13] E.W. Kelley, W.F. Hosford, Trans. Metall. Soc. AIME 242 (1968) 5-13.
- [14] D. Liu, R. Xin, Z. Li, Z. Liu, X. Zheng, Q. Liu, Mater. Sci. Eng. A 646 (2015) 145–153, doi:10.1016/j.msea.2015.08.059.
- [15] W. Wang, W. Zhang, W. Chen, G. Cui, E. Wang, J. Alloy. Compd. 737 (2018) 505–514, doi:10.1016/j.jallcom.2017.12.084.
- [16] Q. Yang, B. Jiang, L. Wang, J. Dai, J. Zhang, F. Pan, J. Alloy. Compd. 814 (2020), doi:10.1016/j.jallcom.2019.152278.
- [17] Q. Wang, B. Jiang, D. Chen, Z. Jin, L. Zhao, Q. Yang, G. Huang, F. Pan, J. Mater. Sci. 56 (2021) 12965–12998, doi:10.1007/ s10853-021-06067-x.
- [18] A. Chapuis, J.H. Driver, Acta Mater. 59 (2011) 1986–1994, doi:10.1016/j.actamat.2010.11.064.
- [19] A.S. Khan, A. Pandey, T. Gnäupel-Herold, R.K. Mishra, Int. J. Plast. 27 (2011) 688–706, doi:10.1016/j.ijplas.2010.08.009.
- [20] N. Stanford, K. Sotoudeh, P.S. Bate, Acta Mater. 59 (2011) 4866–4874, doi:10.1016/j.actamat.2011.04.028.

- [21] C. Yang, B. Shi, Y. Peng, F. Pan, Int. J. Mech. Sci. 160 (2019) 282–297, doi:10.1016/j.ijmecsci.2019.06.046.
- [22] W. Tang, J.Y. Lee, H. Wang, D. Steglich, D. Li, Y. Peng, P. Wu, J. Magn. Alloy. 9 (2021) 927–936, doi:10.1016/j.jma.2020.02.023.
- [23] L. Jin, J. Dong, J. Sun, A.A. Luo, Int. J. Plast. 72 (2015) 218–232, doi:10.1016/j.ijplas.2015.05.010.
- [24] J.C. Baird, B. Li, S. Yazdan Parast, S.J. Horstemeyer, L.G. Hector, P.T. Wang, M.F. Horstemeyer, Scr. Mater. 67 (2012) 471–474, doi:10. 1016/j.scriptamat.2012.06.007.
- [25] W. Wu, A.D. Stoica, D. Yu, M.J. Frost, H.D. Skorpenske, K. An, Crystals 8 (2018) (Basel), doi:10.3390/cryst8090348.
- [26] P.D. Wu, H. Wang, K.W. Neale, Int. J. Appl. Mech. 4 (2012) 1–27, doi:10.1142/S175882511250024X.
- [27] I. Aslam, B. Li, Z. McClelland, S.J. Horstemeyer, Q. Ma, P.T. Wang, M.F. Horstemeyer, Mater. Sci. Eng. A 590 (2014) 168–173, doi:10. 1016/j.msea.2013.10.030.
- [28] B. Yang, Y. Dong, D. Guo, C. Yang, X. Zhang, Y. Peng, L. Wu, B. Shi, Mater. Sci. Eng. A 760 (2019) 415–425, doi:10.1016/j.msea.2019.06. 011.
- [29] L. Wang, G. Huang, T. Han, E. Mostaed, F. Pan, M. Vedani, Mater. Des. 68 (2015) 80–87, doi:10.1016/j.matdes.2014.12.017.
- [30] T. Han, G. Huang, Y. Wang, G. Wang, Y. Zhao, F. Pan, Prog. Nat. Sci. Mater. Int. 26 (2016) 97–102, doi:10.1016/J.PNSC.2016.01.005.
- [31] J. Singh, M.S. Kim, J.H. Lee, H. Guim, S.H. Choi, J. Alloy. Compd. 778 (2019) 124–133, doi:10.1016/j.jallcom.2018.11.138.
- [32] W. Ren, J. Li, R. Xin, Scr. Mater. 170 (2019) 6–10, doi:10.1016/j. scriptamat.2019.05.028.
- [33] G. Huang, L. Wang, H. Zhang, Y. Wang, Z. Shi, F. Pan, Mater. Lett. 98 (2013) 47–50, doi:10.1016/j.matlet.2013.02.055.
- [34] J. Singh, M.S. Kim, J.H. Kang, S.H. Choi, Met. Mater. Int. 25 (2019) 641–656, doi:10.1007/s12540-018-00217-8.
- [35] S.G. Desinghege, P. Hodgson, M. Weiss, J. Mater. Process Technol. 289 (2021) 116951, doi:10.1016/j.jmatprotec.2020.116951.
- [36] J. Singh, M.S. Kim, S.H. Choi, Int. J. Plast. 117 (2019) 33–57, doi:10. 1016/j.ijplas.2018.01.008.
- [37] D. Tang, K. Zhou, W. Tang, P. Wu, H. Wang, Int. J. Plast. 150 (2022) 103180, doi:10.1016/j.ijplas.2021.103180.
- [38] H. Wang, P.D. Wu, C.N. Tomé, Y. Huang, J Mech Phys Solids 58 (2010) 594–612, doi:10.1016/j.jmps.2010.01.004.
- [39] H. Wang, P.D. Wu, C.N. Tomé, J. Wang, Mater. Sci. Eng. A 555 (2012) 93–98, doi:10.1016/J.MSEA.2012.06.038.
- [40] H. Wang, P.D. Wu, C.N. Tomé, J. Wang, Int. J. Solids Struct. 49 (2012) 2155–2167, doi:10.1016/j.ijsolstr.2012.04.026.

- [41] H. Wang, B. Clausen, C.N. Tomé, P.D. Wu, Acta Mater. 61 (2013) 1179–1188, doi:10.1016/j.actamat.2012.10.027.
- [42] H. Wang, P.D. Wu, J. Wang, C.N. Tomé, Int. J. Plast. 49 (2013) 36–52, doi:10.1016/j.ijplas.2013.02.016.
- [43] C. Tome, G.R. Canova, U.F. Kocks, N. Christodoulou, J.J. Jonas, Acta Metall. 32 (1984) 1637–1653, doi:10.1016/0001-6160(84) 90222-0.
- [44] J.D. Eshelby, Proc. R. Soc. Lond. A Math. Phys. Sci. 241 (1957) 376–396, doi:10.1098/rspa.1957.0133.
- [45] C. Sun, Y. Zhou, J. Chen, H. Miao, Exp. Mech. 55 (2015) 1525–1536, doi:10.1007/s11340-015-0055-8.
- [46] S.R. Agnew, in: Advances in Wrought Magnesium Alloys, Elsevier, 2012, pp. 63–104, doi:10.1533/9780857093844.1.63.
- [47] H. Qiao, S.R. Agnew, P.D. Wu, Int. J. Plast. 65 (2015) 61–84, doi:10. 1016/j.ijplas.2014.08.010.

- [48] X.Q. Guo, A. Chapuis, P.D. Wu, S.R. Agnew, Int. J. Solids Struct. 64–65 (2015) 42–50, doi:10.1016/j.ijsolstr.2015.03.012.
- [49] G. Simmons, H. Wang, Single Crystal Elastic Constants and Calculated Aggregate Properties. A Handbook, The MIT Press, 1971.
- [50] R. Cao, Q. Yu, J. Pan, Y. Lin, A. Sweet, Y. Li, R.O. Ritchie, Mater. Today 32 (2020) 94–107, doi:10.1016/j.mattod.2019.09.023.
- [51] X. Wang, L. Jiang, C. Cooper, K. Yu, D. Zhang, T.J. Rupert, S. Mahajan, I.J. Beyerlein, E.J. Lavernia, J.M. Schoenung, Acta Mater. 195 (2020) 468–481, doi:10.1016/J.ACTAMAT.2020.05.021.
- [52] P. Sathiyamoorthi, J. Moon, J.W. Bae, P. Asghari-Rad, H.S. Kim, Scr. Mater. 163 (2019) 152–156, doi:10.1016/J.SCRIPTAMAT.2019.01.016.
- [53] J.Y. Kang, J.G. Kim, S.K. Kim, K.G. Chin, S. Lee, H.S. Kim, Scr. Mater. 123 (2016) 122–125, doi:10.1016/J.SCRIPTAMAT.2016.06.009.
- [54] H. Zhi, C. Zhang, Z. Guo, S. Antonov, Y. Su, Materials 13 (2020) 1–12 (Basel), doi:10.3390/ma13051184.